Seismic observation of tsunami at island broadband stations

Kiwamu Nishida[1], Takuto Maeda[2], Yoshio Fukao[3]

[1]Earthquake Research Institute, University of Tokyo, 1-1-1 Yayoi, Bunkyo-ku, Tokyo 113-0032, Japan

[2]Hirosaki University, Hirosaki, Japan

[3]Japan Agency for Marine-Earth Science and Technology, Yokosuka, Japan

Key Points:

- For quantification of seismic observation of tsunami, we evaluate scattering of an incident tsunami for an axisymmetric structure.
- Ground deformation due to the tsunami loading is modeled using static Green's functions.
- By fitting the modeled displacement to observed seismic data, the incident tsunami is inferred from the seismic observation.

Corresponding author: Kiwamu Nishida, `knishida@eri.u-tokyo.ac.jp`

Abstract

Previous studies have reported seismic observations of tsunami recorded at island broadband stations. Coastal loading by the tsunami can explain them. For further quantification, we model tsunami propagation assuming an axisymmetric structure: a conical island with a flat ocean floor. The total tsunami wavefield can be represented by superposition between an incident tsunami wave and the scattering. The ground deformation due to the total tsunami wavefield at the center is calculated using static Green's functions for elastic half-space with a first-order correction for bathymetry. By fitting the modeled displacement to observed seismic data, we can infer the incident tsunami wave, which can be interpreted as the virtual tsunami amplitude without the conical island. First, we apply this new method to three components of seismic data at a volcano island, Aogashima, for the 2015 Torishima-Oki tsunami earthquake. The estimated tsunami amplitude from the vertical component is consistent with the offshore array observation of absolute pressure gauges close to the island (1.5–20 mHz). The estimated incident azimuth from the three components is also consistent with ray theory. Second, we apply this method to seismic data at four island broadband stations in the Indian ocean for the 2010 Mentawai tsunami earthquake in Indonesia. Despite the limited observed frequency range from 0.5–2.0 mHz, the amplitudes and incident azimuths are consistent with past studies. These observations can complement offshore tsunami observations. Moreover, this method is applicable not only for a tsunami but also for background ocean infragravity wave activity.

1 Introduction

Crustal deformation beneath the ocean due to a massive shallow earthquake generates tsunami (e.g. Satake, 2015). Physically, these are also known as ocean infragravity waves or ocean external gravity waves. Although tsunami amplitudes are usually small in the deep ocean, they increase drastically as tsunami approaches the coast. Such large amplitudes cause severe damage in coastal areas. Understanding tsunami propagation is important for effectively evaluating the risk. Tsunami observations are also crucial for characterizing the source processes of an earthquake (e.g. Satake, Fujii, Harada, & Namegaya, 2013). Observations by offshore ocean bottom pressure gauges (*e.g.* Deep-ocean Assessment and Reporting of Tsunamis (DART) (Bernard & Meinig, 2011)) are typically used for source inversion because of simple wave propagation in the pelagic environment.
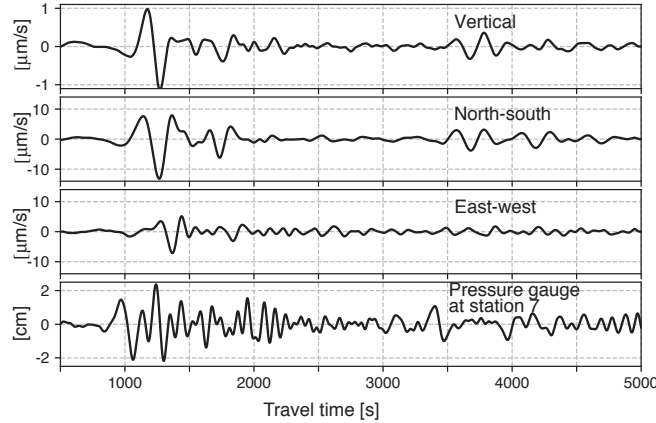
Figure 1. The upper three records show 3 components of the ground velocity recorded by a broadband seismometer at Aogashima (N.AOGF). The lowest record shows tsunami height at an offshore pressure gauge (station 7 shown in Figure 2). All the records are bandpass-filtered from 2 to 20 mHz.

Loading on the seafloor by tsunami causes ground deformation of the ground, and vice versa, which is detectable by land-based broadband seismic stations. For example, when the 2010 Maule earthquake hit Chile, a high-density tiltmeter network in Japan recorded ground tilt motions with a typical period of approximately one hour over a broad inland area facing the Pacific coast (Kimura, Tanaka, & Saito, 2013). Simple 2-D modeling for the deformation induced by the Chilean tsunami explained the observed tilt motions in the Japanese island arc (Kimura et al., 2013). During the 2004 Sumatra–Andaman earthquake, tilt motions from 0.3–0.6 mHz were recorded by a broadband seismometer at Showa station at the mouth of a bay in Antarctica (Nawa et al., 2007), and tilt motions with typical periods of approximately 1000 s were recorded by broadband seismometers at stations on islands in the Indian ocean (Yuan, Kind, & Pedersen, 2005). Although the order of observed amplitudes can be explained by tilt motions caused by tsunami loading, the mechanism is not yet fully understood.

Figure 1 shows an example of broadband seismic records at a volcano island, Aogashima, associated with tsunami when the 2015 Torishima earthquake (see section 5 for details). The observed larger amplitudes in horizontal components suggest the effect of tilt motions is dominant. All the seismic records lack the higher-frequency content.
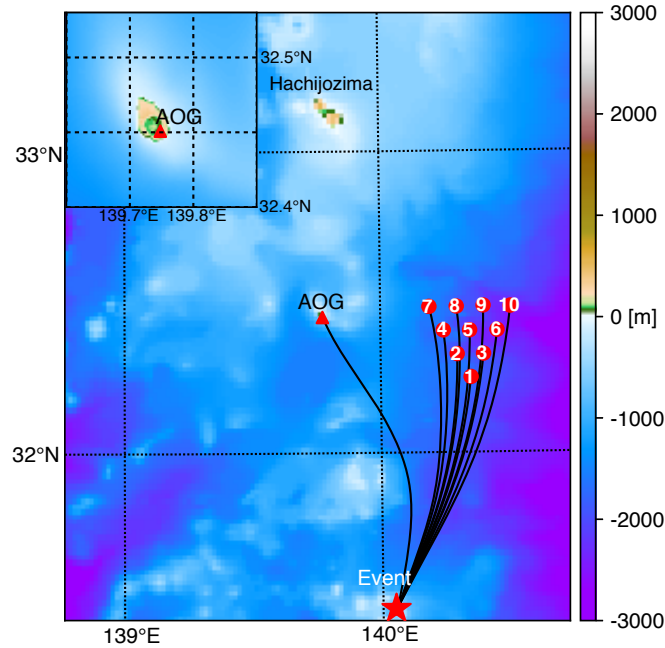
Figure 2. Station distribution of an array of 10 offshore pressure gauges (triangles). The inset shows an enlarged map of Aogashima (AOG). The star symbol shows the hypocenter of the earthquake near Torishima on May 2, 2015. At approximately 33.1°N, Hachijojima north to Aogashima is also shown. The station numbers are shown in red circles.

To quantify ground motions at islands, we model the sloping effects in a semi-analytic manner for an axisymmetric conical island with a flat ocean floor (Fujima & Goto, 1994; Kânoğlu & Synolakis, 1998; Smith & Sprinks, 1975). Although the model is simple, it can express the complex wave propagation close to the shoreline. This simple model can explain the spatial pattern of coastal tsunami amplification around islands.

In section 2, we present a theory of tsunami propagation when an arbitrary tsunami wavefield enters a conical island. In section 3, we then estimate the ground deformation at the center of the island due to tsunami loading, which can be related to the incident tsunami wavefield. In section 4, using the axisymmetric assumption, we propose a new technique for estimating virtual tsunami amplitude without a conical island, which could be a proxy for offshore tsunami amplitude. In section 5, this method is applied to two examples: the 2015 Torishima earthquake in Japan and the 2010 Mentawai tsunami earthquake in Indonesia.

2 Theory of tsunami propagation for a conical island with a flat ocean floor

In this study, we consider scattering of tsunami around an axisymmetric conical island. For simplicity, we assume that the tsunami can be approximated as a linear long-wave because dispersion effects should be less important than topographic effects in this case. Following (Gill, 1982), we consider shallow-water equations derived using the hydrostatic approximation. The displacement amplitude of the sea surface disturbance $\eta(r, \theta; t)$ satisfies the following governing equation in time domain:

$$\frac{\partial^2 \eta(r, \theta; t)}{\partial t^2} = g_0 \nabla_h \left[D(r) \nabla_h \eta(r, \theta; \omega) \right], \tag{1}$$

where r is the radius, θ is the azimuth (Figure 3), g_0 is the gravity constant, ∇_h represents the spatial gradient in 2-D, and $D(r)$ is an axisymmetric water depth given by

$$D(r) = \begin{cases} 0 & \text{if } r < r_0, \\ m(r - r_0) & \text{if } r_0 \leq r < r_1, \\ D_0 & \text{if } r_1 \leq r, \end{cases} \tag{2}$$

where r_1 is the radius of the root of the island, r_0 is the radius of the island, D_0 is the sea surface height of the flat ocean from the sea bottom, and m is the slope given by $D_0/(r_1 - r_0)$. The frequency-domain representation $\eta(r, \theta; \omega)$ satisfies the following equation:

$$-\omega^2 \eta(r, \theta; \omega) = g_0 D(r) \nabla_h^2 \eta(r, \theta; \omega) + g_0 \nabla_h D(r) \cdot \nabla_h \eta(r, \theta; \omega), \tag{3}$$

where ω is the angular frequency.

We note that, for negative frequency, $\eta(r, \theta, -\omega)$ is defined as the complex conjugate by $\eta^*(r, \theta; \omega)$ because the time domain representation should be a real function. A Fourier component at a negative frequency $-\omega$ is, thus, defined by the complex conjugate of that at a positive frequency ω. Here, we use the Fourier convention:

$$F(\omega) = \int_{-\infty}^{\infty} f(t) e^{-i\omega t} dt, \tag{4}$$

where f is an arbitrary function as a function of time, t, and F is its Fourier component.

At high frequency, tsunami velocity $\sqrt{g_0 D(r)}$ near the coast decreases towards zero because the second term of the right-hand side becomes negligible. The coastal low-velocity region traps tsunami energy, which enhances tsunami run-up height (e.g. Liu, Cho, Briggs, Lu, & Synolakis, 1995; Satake, 2015). Zero velocity at the coast makes the governing equation singular. By using the axisymmetric approximation, however, an analytic evaluation of the singularity becomes possible (Fujima & Goto, 1994).

Because the governing equation is axisymmetric, tsunami wavefield $\eta(r, \theta; \omega)$ can

be expanded by a Fourier series with respect to the azimuth, in general, as:

$$\eta(r, \theta; \omega) = \frac{1}{2}\phi_0(r; \omega)$$

$$+ \sum_{n=1}^{\infty} [\phi_n(r; \omega)\cos(n\theta) + \phi_{-n}(r; \omega)\sin(n\theta)], \tag{5}$$

where $\phi_n(r; \omega)$ is the radial function of azimuthal order n. We assume that an arbitrary

incident tsunami wave $\eta^{in}(r, \theta; \omega)$ enters the island and is scattered in the sloping bot-

tom (region II in Figure 3); thus, the total wavefield $\eta(r, \theta; \omega)$ in the flat ocean (region

I in Figure 3) can be represented by superposition between the incident wave and the

scattered wave (Fujima & Goto, 1994; Kânoğlu & Synolakis, 1998; Smith & Sprinks, 1975).

In the following subsections, we evaluate $\phi_n(r; \omega)$ by considering the scattering for an

arbitrary incident wave field using a semi-analytic method (Fujima & Goto, 1994; Kânoğlu

& Synolakis, 1998).

2.1 Incident tsunami wavefield

First, let us consider an arbitrary incident arbitrary wavefield $\eta^{in}(r, \theta; \omega)$ in a flat

ocean without the conical island virtually. The incident wavefield in a flat ocean η^{in} can

be expanded by a Fourier series with respect to the azimuth and Bessel functions of the

first kind with respect to the radial direction as follows:

$$\eta^{in}(r, \theta; \omega) = \frac{1}{2}\zeta_0^{in}(\omega)J_0(k_0 r)$$

$$+ \sum_{n=1}^{\infty} \left[\zeta_n^{in}(\omega)\cos(n\theta) + \zeta_{-n}^{in}(\omega)\sin(n\theta)\right] J_n(k_0 r), \tag{6}$$

where J_n is the nth order Bessel function of the first kind, k_0 is the wavenumber given

by $\omega/\sqrt{g_0 D_0}$, and $\zeta_n^{in}(\omega)$ is the coefficient.

2.2 Wave scattering by a conical island in a flat ocean (I)

The incident wave $\eta^{in}(r, \theta; \omega)$ enters the conical island area and the scattered wave

amplitude is represented by $\eta^{sc}(r, \theta; \omega)$. The total tsunami amplitude η can be written

as

$$\eta(r, \theta; \omega) = \eta^{in}(r, \theta; \omega) + \eta^{sc}(r, \theta; \omega). \tag{7}$$

Let us consider the scattered wavefield $\eta^{sc}(r, \theta; \omega)$ for the flat ocean floor (I) (see

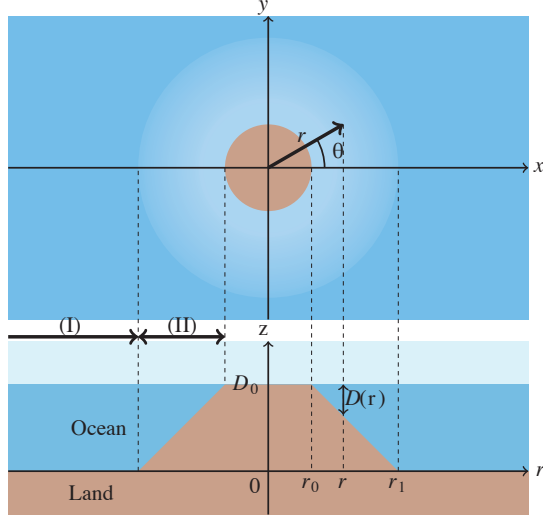Figure 3). The scattered wavefield $\eta^{sc}(r, \theta; \omega)$ can be represented by an outgoing wave

Figure 3. Schematic figure of the conical island. The upper panel shows the plan view of the island, and the lower panel shows the cross-section. The radius on the surface is r_0 and that of the base is r_1.

in the flat ocean according to the causality of the scattered wave. For a positive angular frequency ω, the scattered wavefield can be written as

$$
\eta^{sc}(r, \theta; \omega) = \frac{1}{2} B_0(\omega) \zeta_0^{in}(\omega) H_0^{(2)}(k_0 r)
$$
$$
+ \sum_{n=1}^{\infty} \left[B_n(\omega) \zeta_n^{in}(\omega) \cos(n\theta) + B_{-n}(\omega) \zeta_{-n}^{in}(\omega) \sin(n\theta) \right] H_n^{(2)}(k_0 r), \tag{8}
$$

where $H_n^{(2)}(\omega)$ is the nth order Hankel function of the second kind, which represents outgoing waves, and B_n shows the relative amplitudes of the scattered wave.

In summary, $\phi_n(r; \omega)$ (equation (5)) in this region (I) is given by

$$
\phi_n(r; \omega) = \left(B_n(\omega) H_n^{(2)}(k_0(\omega)r) + J_n(k_0(\omega)r) \right) \zeta_n^{in}(\omega). \tag{9}
$$

We note that the Bessel functions represent the incident waves and the Hankel functions represent the outgoing scattered waves.

2.3 Tsunami wavefield above the sloping bottom in region (II)

For the numerical calculation of $\phi_n(r; \omega)$ within region (II) ($r_0 \leq r \leq r_1$), we define the amplitude A_n and the normalized radial function R_n as:

$$
\phi_n(r; \omega) = A_n(\omega) R_n(r; \omega) \zeta_n^{in}(\omega), \tag{10}
$$

where R_n is normalized so that $R_n(r_0; \omega) = 1$ and A_n is the amplitude factor of ϕ_n at $r = r_0$. Equation (5) in region (II) can be rewritten as follows:

$$\eta(r, \theta; \omega) = \frac{1}{2} A_0(\omega) \zeta_0^{in}(\omega) R_0(r; \omega)$$

$$+ \sum_{n=1}^{\infty} \left[A_n(\omega) \zeta_n^{in}(\omega) \cos(n\theta) + A_{-n}(\omega) \zeta_{-n}^{in}(\omega) \sin(n\theta) \right] R_n(r; \omega). \qquad (11)$$

Inserting $\eta(r, \theta; \omega)$ into the governing equation (equation (3)) leads to the following equation of R_n:

$$\frac{d^2 R_n(r; \omega)}{dr^2} + \left(\frac{1}{r} + \frac{1}{D(r)} \frac{dD(r)}{dr} \right) \frac{dR(r; \omega)}{dr} + \left(\frac{\omega^2}{g_0 D(r)} - \frac{n^2}{r^2} \right) R_n(r; \omega) = 0. \qquad (12)$$

Following Fujima and Goto (1994), we define the following dimensionless parameters, ξ and β, to characterize this system. $\xi(r)$ is the radial phase defined as

$$\xi(r) \equiv \int_{r_0}^{r} k(r') dr' = 2\omega \sqrt{\frac{(r - r_0)}{g_0}} \quad \text{if } r_0 \leq r \leq r_1, \qquad (13)$$

where $k(r)$ is the local wave number given by

$$k(r) \equiv \frac{\omega}{\sqrt{g_0 D(r)}}. \qquad (14)$$

β is the azimuthal number along a circle with a radius of $2r_0$ defined by

$$\beta \equiv \left. \frac{2\pi r}{\lambda(r)} \right|_{r=2r_0}, \qquad (15)$$

where $\lambda(r)$ is wavelength defined by $2\pi/k(r)$. The reason for choosing this radius is discussed in section 6.

The change of variables from r and h to ξ and β leads to the following equation:

$$\frac{d^2 R_n(\xi; \omega)}{d\xi^2} + \left(\frac{2\xi}{\xi^2 + \beta^2} + \frac{1}{\xi} \right) \frac{dR_n(\xi; \omega)}{d\xi} + \left(1 - \left(\frac{2\xi}{\xi^2 + \beta^2} \right)^2 n^2 \right) R_n(\xi; \omega) = 0. \qquad (16)$$

Only in two extreme cases of the radius of the island ($r_0 = 0$ and $r_0 = \infty$) (Fujima & Goto, 1994) can we obtain the analytical solutions of $R(\xi)$, which are crucial for understanding the behavior of $R(\xi)$. Two independent solutions exist according to the governing equation; the only one satisfies the physical requirement, which is a finite amplitude of η at the shoreline. First, let us consider the analytical solution for an infinite radius of the island, which also represents a flat sloping bottom. Because β becomes infinite, $R_n(0)$ is given by

$$R_n(\xi) \sim J_0(\xi). \qquad (17)$$

179   Next, let us consider the analytical solution for the zero island radius case $r_0 = 0$. Be-

180   cause β becomes 0, $R_n(\xi)$ can be given by

$$R(\xi) \sim \frac{J_{\sqrt{1+4n^2}}(\xi)}{\xi}. \tag{18}$$

182   Here, we choose a solution that has a finite amplitude at $\xi = 0$. At $\xi = 0$, only $R_0(\xi)$

183   has a non-zero value, whereas $R_n(0) = 0$ for $n \neq 0$. In general, $R_n(\xi)$ has a signifi-

184   cant value at $\xi = 0$ when $n \leq \beta$ (Fujima & Goto, 1994). Since the evaluation of the

185   ground deformations requires only R_n for $n = 0, \pm 1$, as discussed in the following sec-

186   tions, all the $R_n(\xi)$ have significant values at around $\xi = 0$

187   This ordinary differential equation can be solved using the numerical Livermore Solver

188   for Ordinary Differential Equations (LSODE) (Radhakrishnan & Hindmarsh, 1993). Al-

189   though R_n is integrated from $\xi = 0$ outward with respect to ξ, the governing equation

190   at $\xi = 0$ is a singularity. For this reason, $R_n(\xi)$ is integrated from $\xi = \Delta\xi$ numeri-

191   cally. $R_n(\Delta\xi)$ can be evaluated analytically by the asymptote (Fujima & Goto, 1994).

192    $R_n(\Delta\xi)$ can be represented by Taylor expansion up to the second order when $\Delta\xi \ll 1$

193   and $\beta \neq 0$ (Fujima & Goto, 1994):

$$R_n(\Delta\xi) \approx \left(1 - \frac{1}{4}\Delta\xi^2\right). \tag{19}$$

195   Accordingly, the first order initial boundary conditions of R_n at $\xi = \Delta\xi$ are given by

$$R_n(\Delta\xi) = 1, \tag{20}$$

$$\left.\frac{dR_n(\xi)}{d\xi}\right|_{\xi=\Delta\xi} = -\frac{1}{2}\Delta\xi. \tag{21}$$

2.4 Boundary condition between (I) and (II)

200   We evaluate the boundary condition between (I) and (II) at $r = r_1$ for this equa-

201   tion. Continuity of the amplitude for each azimuthal order, n, and the first derivative

202   at the boundary between regions (I) and (II) leads to the following boundary condition:

$$A_n(\omega)R_n(\xi_1) = J_n(k_0 r_1) + B_n(\omega)H_n^{(2)}(k_0 r_1), \tag{22}$$

$$A_n(\omega)\left(\frac{dR_n(\xi)}{d\xi}\frac{d\xi}{dr}\right)\bigg|_{\xi=\xi_1} = \left.\frac{dJ_n(k_0 r)}{dr}\right|_{r=r_1} + B_n(\omega)\left.\frac{dH_n^{(2)}(k_0 r)}{dr}\right|_{r=r_1}, \tag{23}$$

206   where $\xi_1 \equiv \xi(r_1)$. We can estimate A_n and B_n by solving this equation.

207   Figure 4 shows the induced tsunami wavefield with azimuthal order 0 for the unit

208   amplitude of the incident wave ($\phi_0(r, \omega)/\zeta_0^{in}(\omega)$) at 4 mHz. The parameters are those
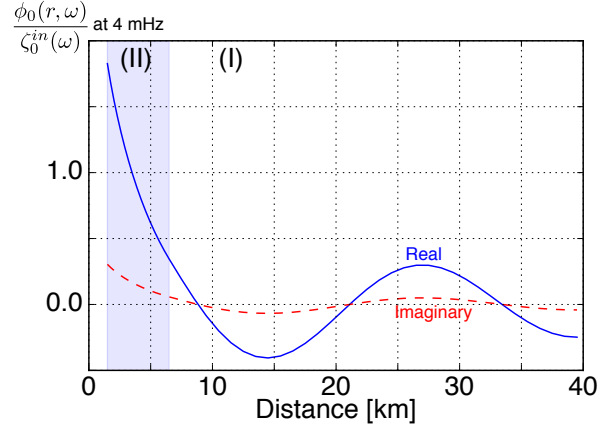
Figure 4. $\phi_0(r;\omega)/\zeta_0(\omega)$ at 4 mHz for Aogashima, the parameters of which are given in Table 1. The blue line shows the real part and the red dashed line shows the imaginary part.

for Aogashima given in Table 1. At approximately $r = r_0$, $\phi_0(r;\omega)/\zeta_0^{in}(r;\omega)$ is larger than 1, which indicates amplification due to confinement along the coast. We discuss this in detail in section 6.

Table 1. Parameters (radius of the island r_0, slope m, and ocean depth D_0) used in this study based on ETOPO1 (Amante & Eakins, 2009). These parameters were estimated by the non-linear least-squares technique using MINPACK (Moré et al., 1984) with trial and error. f_β is a reference frequency used as $\beta = 1$ in equation (15).

station	radius r_0 [km]	slope m	ocean depth D_0 [km]	f_β [mHz]
AOG	1.5	0.20	1.0	2.9
RER	29	0.070	4.2	0.39
AIS	4.9	0.18	2.0	1.5
DGAR	12	0.017	4.2	0.29
CRZF	10	0.034	3.0	0.45

3 Ground deformation by tsunami loading

To estimate ground motions due to tsunami, we assume that they can be represented by static deformation caused by tsunami loading (e.g. Sorrells & Goforth, 1973) because the phase velocity of seismic waves (on the order of 4 km/s) is much faster than

that of a tsunami (on the order of 0.01 km/s) in coastal areas. Loading on the seafloor by the modeled tsunami wavefield is convolved with static Green's functions in a semi-infinite medium with the following correction for bathymetric effects. Because the radius of the island, r_0, is much smaller than r_1 in most cases, we evaluate the deformation, $\boldsymbol{u}(\omega)$, at the center of the island for simplicity. Note that the tilt motion at the center is also calculated because the horizontal component of a broadband seismometer is sensitive to tilt motion in this frequency range (Aki & Richards, 1980).

To evaluate the bathymetric correction for the Green's functions in a semi-infinite medium, the displacement $\boldsymbol{u}(x, y, z)$ and stress $\boldsymbol{\sigma}(x, y, z)$ in a Cartesian coordinate system (x, y, z) is expanded by the powers of slope, m, up to the first order (Segall, 2010; Williams & Wadge, 2000):

$$u_i(x, y, z; \omega) = u_i^{(0)}(x, y, z; \omega) + u_i^{(1)}(x, y, z; \omega)m + \mathcal{O}(m^2), \qquad i = x, y, z \qquad (24)$$

$$\sigma_{ij}(x, y; \omega) = \sigma_{ij}^{(0)}(x, y, z; \omega) + \sigma_{ij}^{(1)}(x, y, z; \omega)m + \mathcal{O}(m^2), \qquad i, j = x, y, z, \qquad (25)$$

where $\mathcal{O}$ indicates "order of", u_i is the displacement, σ_{ij} is the stress, $^{(0)}$ shows the 0th order term, and $^{(1)}$ shows the first order terms. Based on the estimation of the first order terms described in appendix A, the first order terms with respect to the slope, m, becomes comparable to the second order terms. Therefore, we neglect the first order terms below.

The displacement and tilt on the surface ($z = D_0$) and at the center ($x = y = 0$) are corrected for elevation from $z = 0$ as follows:

$$u_\alpha(0, 0, D_0) = u_\alpha^{(0)}(0, 0, 0) - D_0 \left.\frac{\partial u_z^{(0)}}{\partial \alpha}\right|_{z=0}, \qquad \alpha = x, y, \qquad (26)$$

$$u_z(0, 0, D_0) = u_z^{(0)}(0, 0, 0), \qquad (27)$$

$$\left.\frac{\partial u_z}{\partial \alpha}\right|_{x=y=0, z=D_0} = \left.\frac{\partial u_z^{(0)}}{\partial \alpha}\right|_{x=y=z=0}, \qquad \alpha = x, y. \qquad (28)$$

The first-order corrections of horizontal displacement according to the location change are related to the corresponding 0th-order tilt motions. The correction of vertical displacement and tilt motion according to the location change is negligible in the first order because the surface pressure causes a vertical strain $\partial u_z^{(0)}/\partial z = 0$ at the free surface in a half space (Farrell, 1972).

Static Green's functions $g_r^z(r)$, $g_\theta^z(r)$, and $g_z^z(r)$ at a surface point $\boldsymbol{r} = (r, \theta, 0)$ for a vertical force at the origin in a semi-infinite medium are given by (Jaeger, Cook, & Zim-

merman, 2007; Segall, 2010)

$$g_r^z(r) = \frac{1}{4\pi} \frac{1}{\lambda + \mu} \frac{1}{r}, \tag{29}$$

$$g_\theta^z(r) = 0, \tag{30}$$

$$g_z^z(r) = \frac{1}{4\pi\mu} \frac{\lambda + 2\mu}{\lambda + \mu} \frac{1}{r}, \tag{31}$$

where r is the radius in a cylindrical coordinate system (Figure 3), μ, and λ are Lamé's constant of the ground, the superscript on the Green's tensors refers to the direction of the point force, and the subscript refers to the direction of displacement. By convolving forcing by the total tsunami wavefield and the static Green's functions with bathymetric corrections, we can estimate the displacement and tilt at the center.

4 Virtual tsunami amplitude and direction without a conical island

Based on the total tsunami wavefield (section 2) and the Green's functions (section 3), we can relate the ground particle velocity at the center to the incident tsunami using a transfer function. The axisymmetric assumption of the island simplifies the transfer function concerning the azimuthal dependence. By deconvolving the transfer function from observed seismic data in the vertical component, we can infer the incident tsunami amplitude, η^v, at the center assuming that the island is virtually removed. By deconvolving the transfer function from observed seismic data in the horizontal component, we can estimate the spatial gradient of η^v, which shows the propagation direction together with a single plane wave assumption.

4.1 Transfer function of the vertical component

The vertical ground velocity at the origin $v_z(\omega)$ due to the tsunami deformation can be represented by convolution between tsunami loading and the static Green's function as:

$$v_z(\omega) = -\rho g_0 \omega e^{i\pi/2} \int_{r_0}^{\infty} \int_0^{2\pi} \eta(r, \theta; \omega) g_z^z(r) r \, dr \, d\theta, \tag{32}$$

where $v_z(\omega)$ is the particle velocity in the z component given by $i\omega u_z(\omega)$. Let us evaluate the integration using equations (5), (9), and (10). Because the integrand is axisymmetric, the higher order contributions with respect to azimuthal order ($n \geq 1$) such as:

$$-\rho g_0 \omega e^{i\pi/2} \int_{r_0}^{\infty} \phi(r; \omega) g_z^z(r) r \, dr \int_0^{2\pi} \cos(n\theta) d\theta \tag{33}$$

are canceled out. Here, we define the virtual tsunami amplitude, $\eta^v(\omega)$, without the island as

$$\eta^v(\omega) \equiv \eta^{in}(r, \theta; \omega)\big|_{r=0}. \tag{34}$$

The virtual tsunami amplitude can be related to the particle velocity v_z using a transfer function $T_{\eta z}$:

$$v_z(\omega) = T_{\eta z}(\omega)\eta^v(\omega), \tag{35}$$

where $T_{\eta z}(\omega)$ is the transfer function of the tsunami to vertical ground velocity, defined as

$$T_{\eta z}(\omega) \equiv -e^{i\pi/2}\pi\omega\rho g_0 \left(I_1^z(\omega) + I_2^z(\omega)\right), \tag{36}$$

The integrals I_1^z and I_2^z are defined as

$$I_1^z(\omega) \equiv \int_{r_1}^{\infty} \left(B_0(\omega)H_0^{(2)}(k_0 r) + J_0(k_0 r)\right) g_z^z(r)rdr, \tag{37}$$

$$I_2^z(\omega) \equiv \int_{r_0}^{r_1} A_0(\omega)R_0(r)g_z^z(r)rdr, \tag{38}$$

respectively. Figure 5a shows an example of the vertical transfer function $T_{\eta z}(\omega)$ for Aogashima. Below 5 mHz, the transfer function is flat. At 0 frequency, the amplitude and phase of the transfer function can be explained by the theoretical solution for a flat ocean (Ben-Menahem & Singh, 2000) as discussed in section 6. The amplitude decreases with a frequency above 5 mHz because tsunami wavelength becomes smaller than the island scale r_0.

4.2 Transfer function of the horizontal component

Let us consider the transfer function of the horizontal component for tsunami incidence in the same manner. The horizontal ground velocity at the origin $\boldsymbol{v}_h(\omega)$ due to tsunami deformation can be represented by

$$\boldsymbol{v}_h(\omega) \equiv \begin{pmatrix} v_x(\omega) \\ v_y(\omega) \end{pmatrix} = -\rho g_0 \omega e^{i\pi/2} \int_{r_0}^{\infty} \int_0^{2\pi} \eta(r, \theta; \omega) \left(g_r^z - D_0\frac{\partial g_z^z}{\partial r}\right) \begin{pmatrix} -\cos\theta \\ -\sin\theta \end{pmatrix} rdrd\theta. \tag{39}$$

Because $\cos\theta$ and $\sin\theta$ have orthogonality with respect to the azimuthal integration, only $n \pm 1$ in terms of η contributes to the integration, as follows:

$$\begin{pmatrix} v_x(\omega) \\ v_y(\omega) \end{pmatrix} = \frac{i}{2}T_{\eta h}(\omega) \begin{pmatrix} \zeta_1^{in} \\ \zeta_{-1}^{in} \end{pmatrix} = i\frac{T_{\eta h}(\omega)}{k_0} \left.\nabla_h \eta^{in}(r, \theta; \omega)\right|_{r=0}. \tag{40}$$

304   Here, $T_{\eta h}(\omega)$ is given by,

$$T_{\eta h}(\omega) = 2\pi\omega\rho g_0 \left(I_1^h(\omega) + I_2^h(\omega) \right), \qquad (41)$$

306   where integrals I_1^h and I_2^h are defined as

$$I_1^h(\omega) \equiv \int_{r_1}^{\infty} \left(B_1(\omega)H_1^{(2)}(k_0 r) + J_1(k_0 r)) \right) \left(g_r^z - D_0 \frac{\partial g_z^z}{\partial r} \right) r dr, \qquad (42)$$

$$I_2^h(\omega) \equiv \int_{r_0}^{r_1} A_1(\omega)R_1(r) \left(g_r^z - D_0 \frac{\partial g_z^z}{\partial r} \right) r dr. \qquad (43)$$

310   The spatial gradient of the surface displacement $\nabla_h \eta|_{r=0}$ can be related to the flow rate,

311    $\mathbf{Q}$ (Satake, 2015), at the origin defined as

$$\mathbf{Q} = \int_{D_0-D(r)}^{D_0} \boldsymbol{v}_h dz = \frac{ig_0}{\omega}, \nabla_h \eta^{in}\big|_{r=0} \qquad (44)$$

313    $D(r)$ is water depth at r and D_0 is water depth of the flat ocean floor (Figure 3).

314   For simplicity, we assume that η can be represented by a single plane wave inci-

315   dence with the relative travel time, $\mathcal{T}(r,\theta)$, to the origin. The gradient can be written

316   as

$$\nabla_h \eta^{in}(r,\theta;\omega) = -i\omega\eta^{in}(0,\theta;\omega)\nabla_h\mathcal{T}(r,\theta) = \eta^{in}(0,\theta;\omega)(-ik_0)\boldsymbol{e}_r, \qquad (45)$$

318   where $\boldsymbol{e}_r$ is the propagation direction of the tsunami. Then, we obtain the following re-

319   lationship:

$$\boldsymbol{v}_h(\omega) = T_{\eta h}(\omega)\eta^v(\omega)\boldsymbol{e}_r. \qquad (46)$$

321    $T_{\eta h}$ represents the transfer function from the tsunami incidence to horizontal ground ve-

322   locity at the center. This result shows that the observed ground velocity is parallel to

323   the tsunami propagation direction under the single plane-wave assumption. Figure 5a

324   shows an example of the horizontal transfer function $T_{\eta z}(\omega)$ for Aogashima. The trans-

325   fer function has a broad peak at 5 mHz. At 0 frequency, the amplitude and phase of the

326   transfer function can be explained by the theoretical solution for a flat ocean (Ben-Menahem

327   & Singh, 2000) as discussed in section 6. The amplitude also decreases with a frequency

328   above 5 mHz.

329   Below 1 mHz, tilt motion induced by tsunami is dominant in the horizontal com-

330   ponent of seismic sensors (Kimura et al., 2013; Nawa et al., 2007). The horizontal ac-

331   celeration contribution due to tilt motion ($\nabla_h u_z$, where u_z is the vertical displacement)

332   is given by $g_0\nabla_h u_z$ (e.g. Rodgers, 1968; Wielandt & Forbriger, 1999). Then, the tilt mo-

tion at the origin, $v(\omega)$, due to deformation by the tsunami can be represented by

$$\boldsymbol{v}_h^{tilt}(\omega) = \frac{g_0 \nabla_h u_z}{i\omega} = \frac{-\rho g_0}{i\omega} \int_{r_0}^{\infty} \int_0^{2\pi} \eta(r,\theta;\omega) \frac{\partial g_r^z}{\partial r} \begin{pmatrix} -\cos\theta \\ -\sin\theta \end{pmatrix} r dr d\theta. \tag{47}$$

The higher order contributions ($n \neq \pm 1$) are again canceled out.

$$\boldsymbol{v}^{tilt}(\omega) = \frac{i}{2} T_{\eta h}(\omega) \begin{pmatrix} \zeta_1^{in} \\ \zeta_{-1}^{in} \end{pmatrix} = i \frac{T_{\eta h}^{tilt}(\omega)}{k_0} \left. \nabla_h \eta^{in}(r,\theta;\omega) \right|_{r=0}. \tag{48}$$

Here, the transfer function due to tilt, $T_{\eta h}^{tilt}(\omega)$, of the tsunami to horizontal ground velocity is given by,

$$T_{\eta h}^{tilt}(\omega) = \frac{2\pi \rho g_0}{\omega} \left(I_1^t(\omega) + I_2^t(\omega) \right), \tag{49}$$

where integrals I_1^t and I_2^t are defined by

$$I_1^t(\omega) \equiv \int_{r_1}^{\infty} \left(B_1(\omega) H_1^{(2)}(k_0 r) + J_1(k_0 r) \right) \frac{\partial g_h^r(r)}{\partial r} r dr, \tag{50}$$

$$I_2^t(\omega) \equiv \int_{r_0}^{r_1} A_1(\omega) R_1(r) \frac{\partial g_z^z(r)}{\partial r} r dr. \tag{51}$$

Then, we also obtain the following relationship:

$$\boldsymbol{v}_h^{tilt}(\omega) = T_{\eta h}^{tilt}(\omega) \eta^v(\omega) \boldsymbol{e}_r. \tag{52}$$

Figure 5b shows that the tilt effects of the horizontal transfer function are dominant, specifically at low frequencies. Below 1 mHz, the transfer function approaches the theoretical solution for a flat ocean (Ben-Menahem & Singh, 2000), which is proportional to ω^{-1}. With increasing frequency, the contribution of the tilt effect decreases. Although the amplitudes of horizontal components are an order of magnitude larger than those of vertical components, the estimated virtual tsunami amplitude from horizontal components is more ambiguous. This is because tilt motions, which are the spatial derivative of vertical motion, are more sensitive to small-scale bathymetric changes and crustal heterogeneity.

5 Comparison with observations

During huge shallow earthquakes, the horizontal components of broadband seismometers located on an island often record tilt motion associated with tsunami (e.g., the 2004 Sumatra earthquake (Yuan et al., 2005)), although the contribution of low-frequency seismic waves excited by the earthquake (Kimura et al., 2013; Yuan et al., 2005) disturbs
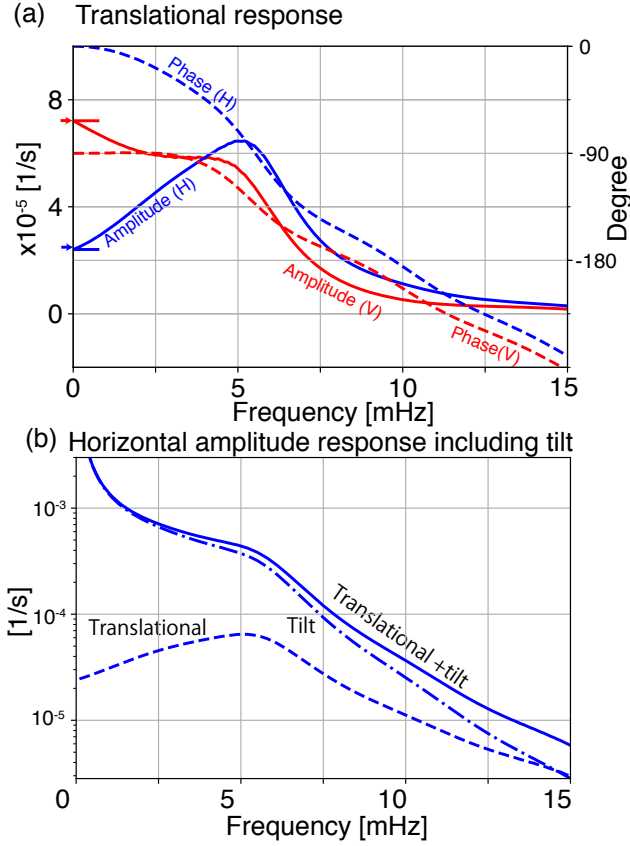
Figure 5. (a) Transfer function of translational motions against frequency. The dashed lines show the phases and the solid lines show the amplitudes, where (V) in the figure represents the vertical component and (H) shows the horizontal component. The red and blue lines show the vertical and horizontal transfer functions, respectively. Red and blue arrows at 0 mHz show theoretical amplitudes for a flat ocean (Ben-Menahem & Singh, 2000) in vertical and horizontal components respectively. The phase shift can be explained by the arrival delay (approximately 70 s). (b) Amplitude of the transfer function of the horizontal component against frequency according to the contribution of translational motion, tilt motion, and both. The contribution of tilt motion is dominant below 5 mHz. We note that phases of the transfer function due to tilt are analytically the same as those of horizontal transfer function at all frequencies.

the tsunami signal. The amplitudes of vertical components are too small to detect because the vertical response is much smaller than the tilt response, as shown in Figure 5.

In order to suppress the noise, we apply this method to tsunami earthquakes, which cause a much larger tsunami than expected from the seismic moment. We determine the virtual tsunami amplitude and direction for two tsunami earthquakes: (1) the 2015 volcanic tsunami earthquake near Torishima, Japan, and (2) the 2010 Mentawai tsunami earthquake in Indonesia. These results are verified by ray theory and other geophysical observations.

5.1 Torishima 2015 Earthquake in Japan

A compensated-linear-vector-dipole (CLVD) type earthquake occurred on May 2, 2015, near Torishima island, Izu–Bonin arc, Japan (Figure 2), generating an abnormally large tsunami (*e.g.* 0.5 m at Hachijozima 180 km north of the epicenter) for the moment magnitude of M_w 5.7, determined by the U.S. Geological Survey. The tsunami was caused by large deformation in a shallow part of a submarine volcanic body (Fukao et al., 2018). A triangular array of ocean bottom pressure (OBP) gauges recorded an off-shore tsunami (Sandanbata et al., 2017). They were deployed 100 km northeast of the epicenter with a station separation of approximately 10 km (Figure 2). All tsunami waveforms with amplitudes of approximately 2 cm are similar to each other (Figure 6). A tsunami earthquake with a surface wave magnitude of Ms 5.6 in the same area occurred on June 13, 1984 (Kanamori, Ekström, Dziewonski, Barker, & Sipkin, 1993; Satake & Kanamori, 1991); their focal mechanisms suggest magma injection with the submarine volcano (Fukao et al., 2018; Kanamori et al., 1993).

At Aogashima island, close to the array, a broadband seismometer (STS2) of F-net (Okada et al., 2004) was deployed by the National Research Institute for Earth Science and Disaster Prevention (NIED). Because seismic waves from tsunami earthquakes were relatively small at a low-frequency of 1.5-20 mHz, the broadband seismometer recorded clear ground motions associated with the tsunami (Figure 1). We can compare the estimated virtual tsunami amplitudes from the seismic observations with near deep ocean bottom pressure gauge.
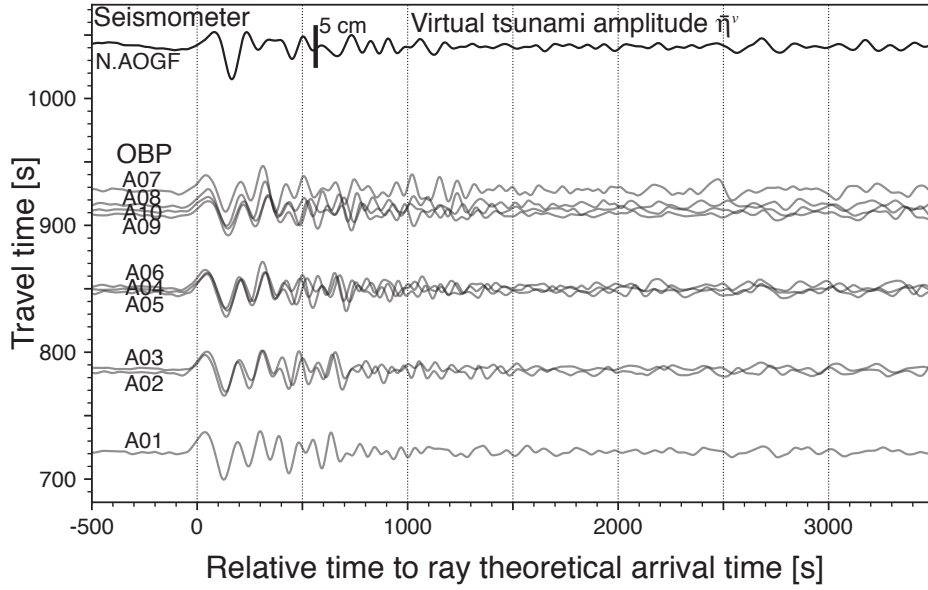
Figure 6. Estimated virtual tsunami amplitude with array observations by absolute pressure gauges. The vertical axis shows travel time predicted by ray theory and the horizontal axis shows relative time to the ray theoretical arrival time. Here, travel times are calculated by fast marching (Rawlinson, 2005; Rawlinson & Sambridge, 2005) using the long wave approximation. The uppermost record shows the virtual tsunami amplitude estimated from the vertical ground velocity at Aogashima (N.AOGF). The lower record shows 10 records of ocean bottom pressure gauges. These records are bandpass filtered from 1.5 to 20 mHz (4th order Butterworth, zero phase). The amplitude scales are the same throughout all records. The maximum amplitudes are approximately 2 cm.

³⁹⁰   Using the vertical component of the broadband seismometer, we infer the virtual

³⁹¹ tsunami amplitude. The modeled parameters of the conical island are given in Table (1).

³⁹² Using the transfer function, $T_{\eta z}(\omega)$, shown by Figure 5a, we estimate the virtual tsunami

³⁹³ amplitude $\bar{\eta}^v(\omega)$ by deconvolution:

$$\bar{\eta}^v(\omega) = \frac{T_{\eta z}^*(\omega)}{T_{\eta z}^*(\omega)T_{\eta z}(\omega) + w} v_z(\omega), \tag{53}$$

³⁹⁵ where w is the water level, which is 5×10^{-3} of the squared amplitude of $T_{\eta z}$ at 5 mHz.

³⁹⁶ The $\bar{\eta}^v$ is converted in time domain. Figure 6 shows the comparison of $\bar{\eta}^v(t)$ with ob-

³⁹⁷ served tsunami amplitudes by the pressure gauges against the relative travel time. The

³⁹⁸ estimated amplitude of approximately 2.5 cm and the relative travel times are consis-

³⁹⁹ tent with the offshore observations. The ray theoretical arrival times should coincide with

–18–

the peak time, but the figure shows slight delays in the peak time, which are attributed

to dispersion due to the finite wavelength. This result verifies the feasibility of this method.

Next, let us consider the propagation direction from the observed horizontal components shown in Figure 5b. Using the transfer function, $T_{\eta h}$, for horizontal components, the tsunami amplitude with a propagation direction of $(\bar{\eta}_x^v, \bar{\eta}_y^v)$ can be defined as,

$$\begin{pmatrix} \bar{\eta}_x^v(\omega) \\ \bar{\eta}_y^v(\omega) \end{pmatrix} \equiv \frac{T_{\eta h}^*}{T_{\eta h}^*(\omega)T_{\eta h}(\omega) + w} \begin{pmatrix} v_x(\omega) \\ v_y(\omega) \end{pmatrix}, \tag{54}$$

where w is the water level, which is 1×10^{-3} the squared amplitude of $T_{\eta h}$ at 5 mHz. With the single plane wave assumption, $(\bar{\eta}_x^v, \bar{\eta}_y^v)$ can be interpreted as $\eta^{in}\boldsymbol{e}_r$ (equation (46)). Figure 7a shows the comparison among $\bar{\eta}_x^v$, $\bar{\eta}_y^v$, and $\bar{\eta}^v$. The waveforms at approximately 1000 s are consistent with each other.

The particle motions of the horizontal components (Figure 7b) shows a linear polarization, which is consistent with the ray path shown in Figure 2. The consistency suggests that the assumptions related to the approximations of the conical island and the single plane wave are appropriate. Although the horizontal amplitude is slightly larger than the vertical amplitude, the discrepancy can be attributed to the slightly off-center station to the southwest. Phases of the later arrival at approximately 3000 s in Figure 7 are different in different components because they are composed of multiple scattering waves.

To quantitatively estimate the propagation direction, we assume that the virtual tsunami amplitude is given by $\bar{\eta}^v$ from the vertical component. Then, equation (46) leads to

$$\begin{pmatrix} \bar{\eta}_x^v(\omega) \\ \bar{\eta}_y^v(\omega) \end{pmatrix} = \bar{\eta}^v \begin{pmatrix} \sin\varphi \\ \cos\varphi \end{pmatrix}, \tag{55}$$

where φ is the propagation azimuth, which, in this case, can be estimated by

$$\varphi = \frac{\pi}{2} - \arctan 2\left(\int_{t_0}^{t_1} \bar{\eta}_y^v(t)\bar{\eta}^v(t)dt, \int_{t_0}^{t_1} \bar{\eta}_x^v(t)\bar{\eta}^v(t)dt\right), \tag{56}$$

where $\arctan 2$ is 2-argument arc-tangent,t_0 is 0 s, and t_1 is 5000 s. The red arrow in Figure 7 shows the propagation direction φ, whose length shows the root mean squared amplitude from 0 to 5000 s. Because the integration in the above equation, which represents covariance between the vertical and horizontal components, suppress incoherent parts, which originate from the higher noise level and scattered wavefield, the estima-
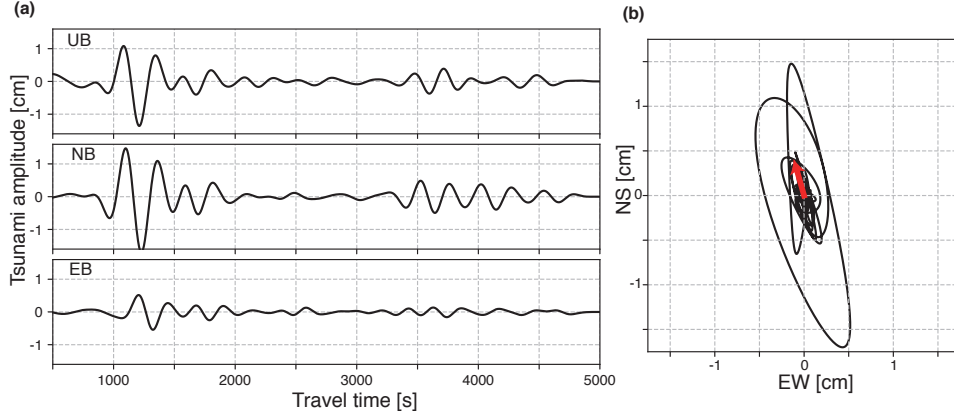
Figure 7. (a) The three components of the estimated tsunami waveform. The first is 2–5 mHz with a 6th order Butterworth filter. (b) Particle motions of the horizontal components from 2 to 5 mHz. The red arrow shows the estimated propagation direction with root mean squared amplitudes from 0 to 500 s.

tion is expected to be robust. Figure 8 shows the comparison between the estimated azimuth and the ray azimuth at the station. This figure shows that they are consistent within 10 degrees. We also note that the above method enables us to estimate the propagation direction without introducing a 180° uncertainty (e.g. Takagi, Nishida, Maeda, & Obara, 2018).

5.2 Mentawai 2010 in Indonesia

The 2010 Mentawai earthquake (Mw 7.8) caused a destructive tsunami in the Mentawai Islands, west of Sumatra in Indonesia (Satake, Nishimura, et al., 2013). The tsunami amplitude reached 9.3 m on the west coasts of North and South Pagai Island. Seismological data analyses show that the earthquake was a tsunami earthquake (e.g. Lay et al., 2011). For the analysis, we use four broadband stations located on islands DGAR, RER, CRZF, and AIS shown in Figure 9. For the estimation of tsunami amplitude, we use the water level (see equations (53) and (54)), which is 5% of the maximum squared amplitude in a frequency range from 0.7 to 2 mHz.

Because most island radii (Table 1) are larger than that of Aogashim, as shown in Figure 10, their transfer functions are not sensitive to tsunami above 1 mHz, as shown in Figure 11. Hence, we focus on a signal with a typical frequency of 1 mHz. The esti-
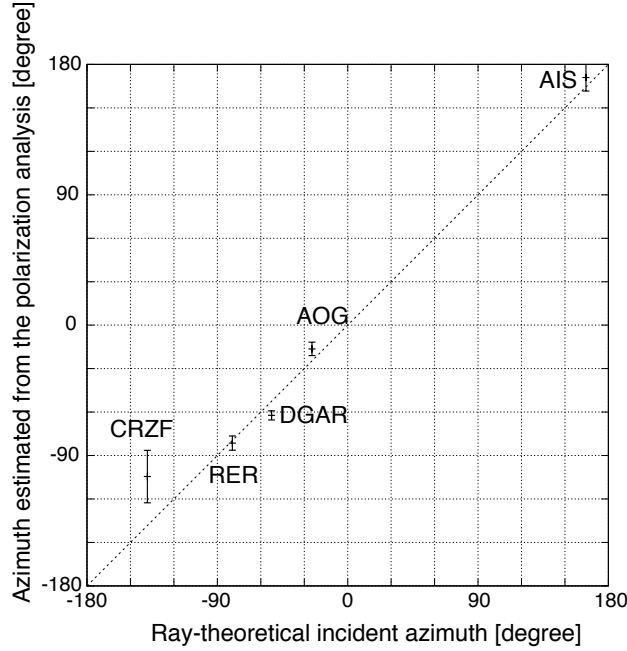
Figure 8. Propagation azimuths at stations. The horizontal axis shows the propagation azimuths estimated by this method utilizing broadband seismic data, whereas the vertical axis shows azimuths based on ray theory. To estimate the error of the propagation azimuth, we made 10^5 bootstrap samples and We estimated the error bars of 1σ by the use of moving block bootstrap resampling (Vogel & Shallcross, 1996). We made 10^5 bootstrap samples with a block length of 50 s at Aogashima and that of 100 s at the other stations respectively.

mated virtual tsunami amplitudes were 0.4 cm at DGAR, 1.3 cm at AIS, 0.9 cm at CRZF, and 0.6 cm at RER. Arrival times of the estimated waveforms are consistent with the ray theoretical values. The arrival time at DGAR is advanced because the simple symmetric model is too simple to model a large island with a larger root size r_1 of approximately 260 km (see Table 1). Although DART station 5601 recorded a maximum tsunami amplitude of 1 cm (Satake, Nishimura, et al., 2013), it is located 1,600 km south to the epicenter. Because there are no offshore stations close to the four seismic broadband stations, we compare the virtual tsunami heights $\bar{\eta}^v$ with numerical results by NOAA Center for Tsunami Research, which are maximum tsunami heights at an offshore points close to the stations based on the NOAA forecast method using MOST model with the tsunami source inferred from DART data (Gica, Spillane, Titov, Chamberlin, & Newman, 2008).

The calculated maximum wave heights of about 5 mm for RER, about 14 mm for AIS, about 14 mm, and about 8 mm for CRZF are consistent with our estimations.
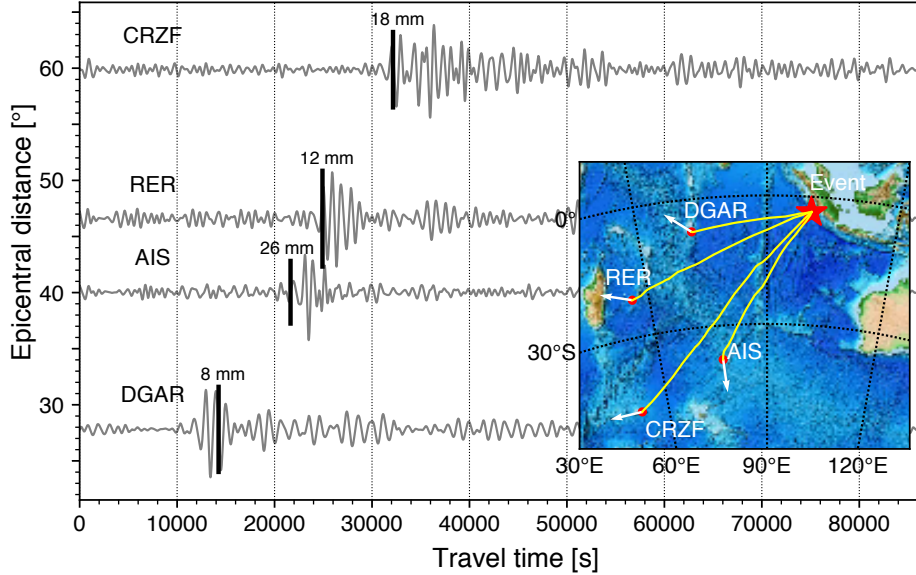

Figure 9. Virtual tsunami amplitudes at four stations for the 2010 Mentawai earthquake (Oct 25, 2010). 0.7–2 mHz (order 6). The map in the inset shows the station locations and the earthquake location. The bold black bars show the corresponding ray theoretical arrival times with amplitude scales.

The map in Figure 9 shows the estimated propagation directions using three components of broadband seismometers, as shown in the previous subsection. Although the estimated azimuths are slightly different from the ray paths on this large scale, the difference can be attributed to strong refraction close to the islands. Indeed, the relationship between the propagation azimuths estimated from the seismic stations can be explained by the azimuths predicted by ray theory, as shown in Figure 8. These are consistent with ray paths within 10 degrees except for CRZF. The deviation could be explained by scattering due to the neighboring island (Figure 10), which may break the single plane wave approximation.
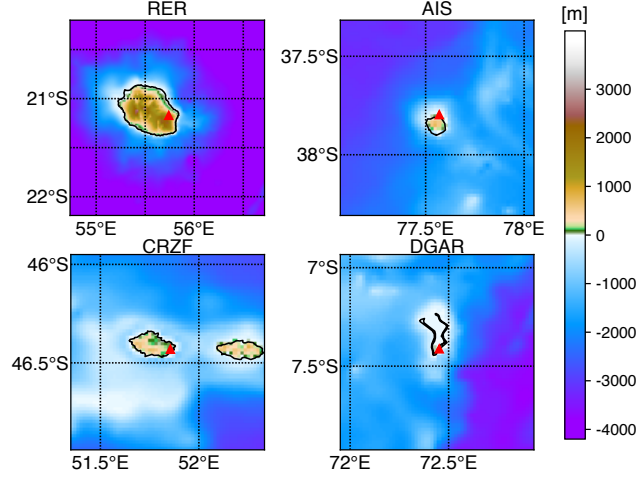
Figure 10. Enlarged maps of the islands. Stations are indicated by red triangles.

6 Characteristics of the transfer function according to the slope and radius

Tsunami trapping in the coastal slope of a conical island is crucial for characterizing the transfer functions. This section describes the amplification characteristics due to trapping in coastal areas, where the trapping condition (Longuet-Higgins, 1967) is given by,

$$\frac{\partial}{\partial r}\left(\frac{D(r)}{r^2}\right) \geq 0. \tag{57}$$

For the case of a conical island, the condition can be simplified as

$$r \leq 2r_0. \tag{58}$$

This relationship indicates that a larger conical island will trap more inshore areas.

β defined in equation (15) is crucial for characterizing the trapping effect. β can be interpreted as the ratio of the circumference, $4\pi r_0$ at $r = 2r_0$, to the wavelength, λ. In other words, β shows the azimuthal number of the trapped mode. Here, we define the cut-off frequency f_β as $\beta = 1$. Above this frequency, the tsunami is trapped in inshore areas. f_β is also a good proxy for ground deformation at the center because the deformation becomes significant when the radius of the island becomes larger than the wavelength. Consequently, the ground deformation becomes small with increasing frequency above the frequency. The f_β value, therefore, characterizes the cut-off frequency of the transfer functions. Table 1 shows f_β for the islands, which correspond to the cut-off frequency shown in Figure 11.
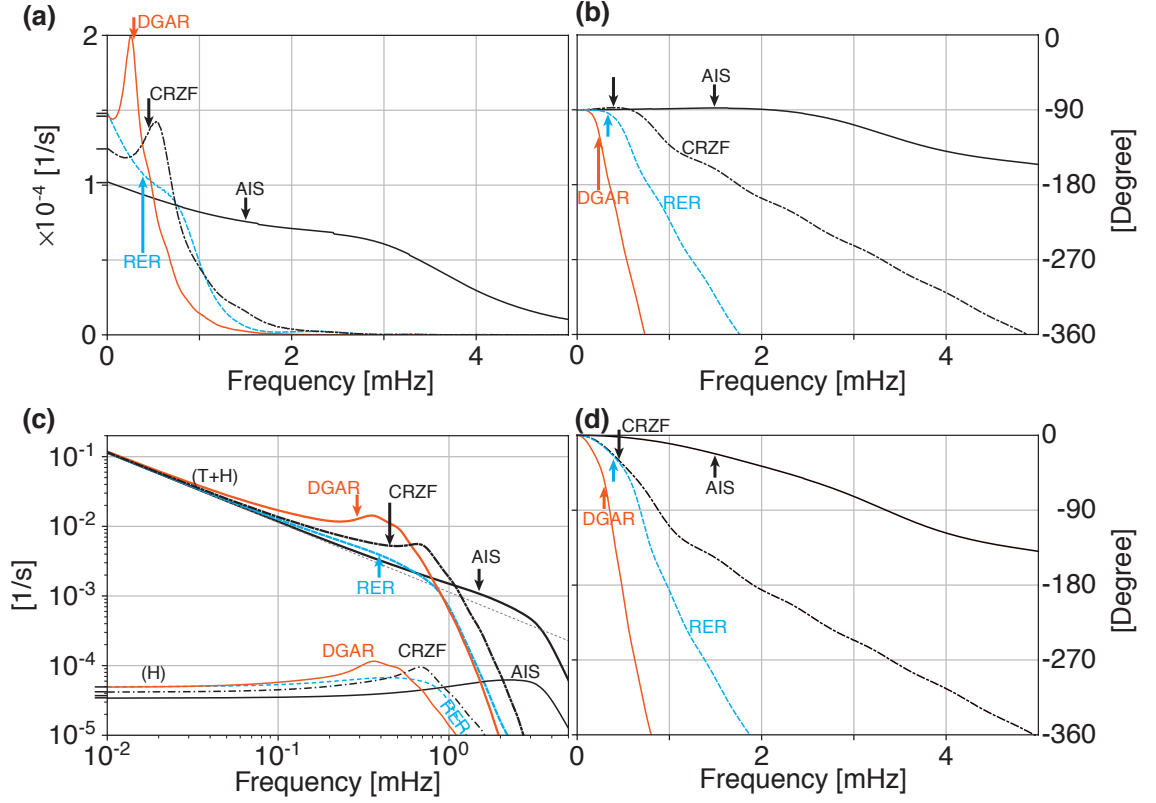
Figure 11. (a) Amplitudes of transfer functions for vertical components against frequency at the four broadband stations, composed of one IRIS IDA station, DGAR (Diego Garcia, Chagos islands), and three GEOSCOPE stations RER (La Réunion Island, France), CRZF (Port Alfred - Ile de la Possession - Crozet Islands, France), and AIS (Nouvel Amsterdam, TAAF, France). Station locations are shown in Figure 9. Black tick marks at 0 mHz show theoretical amplitudes for a flat ocean (equation (59)) in vertical components. The f_β values are shown by arrows. (b) Phases of the transfer functions for vertical components against frequency. (c) Amplitudes of transfer functions for horizontal components against frequency. Labels (H) shows the horizontal components due to translational motion, and (H+T) shows the horizontal component including the tilt effect. Black tick marks at 0 mHz show the theoretical amplitudes for a flat ocean (equation (60)) in horizontal components, and the straight dot-line in gray shows the theoretical amplitudes caused by the tilt motion for a flat ocean (equation (61)). (d) Phases of the transfer functions for horizontal components against frequency.

488   With a smaller slope m, more tsunami energy is trapped in the inshore area due

489 to the slow propagation speed. In this case, the transfer function exhibits a peak at ap-

490 proximately f_β. The translational transfer functions of DGAR and CRZF with smaller

491 slope, m, show peaks at approximately f_β.

492   At much lower frequencies than f_β, we can neglect scattering by the island because

493 the wavelength of the tsunami becomes much larger than the island scale. Moreover, the

494 contribution of ground deformation in the inshore area becomes negligible. In this limit,

495 the transfer functions are approximated by those of a semi-infinite medium loaded by

496 pressure fluctuations on the surface given by Ben-Menahem and Singh (2000):

497
$$\lim_{\omega \to 0} T_{\eta z}(\omega) = \frac{e^{-i\pi/2}\sqrt{g_0 D_0}}{2(\lambda + \mu)} \frac{\lambda + 2\mu}{\mu} \rho g_0, \tag{59}$$

498
$$\lim_{\omega \to 0} T_{\eta h}(\omega) = \frac{\sqrt{g_0 D_0}}{2(\lambda + \mu)} \rho g_0, \tag{60}$$

499
500
$$\lim_{\omega \to 0} T_{\eta h}^{tilt}(\omega) = \frac{\lambda + 2\mu}{2(\lambda + \mu)\mu} \rho \frac{g_0^2}{\omega}. \tag{61}$$

501 Figure 5a and Figure 11 show that the transfer functions approaching zero frequency also

502 approach the above values. Figure 11 (d) also shows that $T_{\eta h}^{tilt}(\omega)$ actually approaches

503 equation (61) in the low frequency limit.

504   At frequencies higher than about $10f_\beta$, the wavelength of tsunami becomes much

505 smaller than the island scale. Consequently, the scattering by small scale bathymetric

506 changes breaks the basic assumption of this method. Thus, f_β could be a proxy for the

507 characteristics when evaluating the transfer function.

7 Potential applications for ocean infragravity waves

509   Although tsunami in this frequency range is ocean infragravity waves excited by

510 an earthquake, ocean infragravity waves are also excited by the other geophysical pro-

511 cesses. For example, they are excited persistently along shorelines by incident ocean swell

512 through nonlinear processes and travel across the ocean with a typical height on the or-

513 der of 1 cm in pelagic regions (Rawat et al., 2014; Tonegawa et al., 2018). The background

514 ocean infragravity-wave activities are also key for understanding background seismic wave-

515 fields know as seismic hum because they are the primary excitation source (Ardhuin, Gualtieri,

516 & Stutzmann, 2015; Nishida, 2013, 2017; Rhie & Romanowicz, 2004). Observed equipar-

517 tition of energy between Love and Rayleigh waves (Fukao, Nishida, & Kobayashi, 2010;

518 Nishida, Kawakatsu, Fukao, & Obara, 2008) suggests a topographic coupling between

ocean infragravity waves and seismic surface waves. Seismic observations at island broadband stations could be used to understand the excitation mechanisms because modeling of ocean infragravity waves requires further researches (Ardhuin et al., 2015; Ardhuin, Rawat, & Aucan, 2014).

Our proposed technique for estimating virtual tsunami amplitude is applicable not only for tsunami but also for random wavefields of the background ocean infragravity waves. Seismic observations at islands could elucidate ocean infragravity wave activities. The wave action model WAVEWATCH III has recently been extended from the swell band to ocean infragravity waves (Ardhuin et al., 2014) and recovers the observed energy of wave height within 50%. Our method could be used to improve such models.

8 Conclusions

In this study, we consider that an arbitrary tsunami in a flat ocean floor enters a conical island. The scattering wavefield is evaluated using a semi-analytical method, which is an extension of the theory of Fujima and Goto (1994). Then, we calculate ground deformation due to tsunami loading at the center of the conical island using static Green's functions with a first-order correction for bathymetry. In this formulation, the ground motions can be represented by convolution between the transfer functions and the incident tsunami amplitudes at the station. The transfer functions are characterized by a cutoff frequency, f_β, and they approach those given by Ben-Menahem and Singh (2000) for a semi-infinite medium loaded by pressure on the surface without an island. By deconvolving the transfer functions from seismic data, we can infer the incident tsunami wavefield, which can be interpreted as the virtual tsunami amplitude without the island. Thus, we propose a new technique for estimating the virtual tsunami amplitude and propagation direction from seismic data using the assumption of a single plane wave.

First, we apply this technique to seismic records from Aogashima volcanic island when the Torishima Oki earthquake hit on May 2, 2015. The estimated tsunami amplitude is quantitatively consistent with an array observation of pressure gauges close to the island from 1.5 to 20 mHz. The incident angle estimated from the seismic data is also consistent with the ray-theoretical value. We also apply this method to seismic data at four broadband stations located on islands in the Indian ocean for the tsunami earthquake in Mentawai, Indonesia on October 25, 2010. Although the observed frequency

550 range is limited from 0.5 to 2.0 mHz, the incident angles are consistent with ray theo-

551 retical values. This method can, therefore, complement offshore tsunami observations.

552   Because this technique is formulated for an arbitrary incident wavefield, it could

553 be employed not only for tsunami but also for background ocean infragravity waves, which

554 are excited along shorelines by incident ocean swell through nonlinear processes. Fur-

555 ther research should develop this method in order to elucidate background ocean infra-

556 gravity wave activities using broadband seismic stations located on islands.

A Correction of ground deformation for tilt

Following Segall (2010), we estimate the first order correction of displacements $u_i^{(1)}$ ($i = x, y, z$) for the bathymetry as induced displacement by the first order stress $\sigma_{ij}^{(1)}$ in a cylindrical coordinate (r, θ, z), given by

$$\sigma_{zz}^{(1)} = 0, \tag{A.1}$$

$$\sigma_{rz}^{(1)} = -\frac{dh}{dr}(\sigma_{zz}^{(0)} - \sigma_{rr}^{(0)}), \tag{A.2}$$

$$\sigma_{\theta z}^{(1)} = -\frac{dh}{dr}\sigma_{r\theta}^{(0)} \tag{A.3}$$

at $z = 0$. Here, the 0th-order terms in Cartesian coordinates satisfy

$$\frac{\partial \sigma_{ij}^{(0)}}{\partial x_j} = 0 \tag{A.4}$$

with boundary conditions given by

$$\sigma_{zz}^{(0)} = -p(x, y), \sigma_{zx}^{(0)} = 0, \sigma_{zy}^{(0)} = 0. \tag{A.5}$$

We note the following relationships:

$$\left.\frac{\partial \sigma_{rz}^{(0)}}{\partial z}\right|_{z=0} = \left.\frac{\partial \sigma_{\theta z}^{(0)}}{\partial z}\right|_{z=0} = \left.\frac{\partial \sigma_{zz}^{(0)}}{\partial z}\right|_{z=0} = 0, \tag{A.6}$$

on the free surface of the island. This result is obtained by representing the stress in terms of the Newtonian potential functions (Love, 1929, section 1.1).

The first order displacement can be calculated by convolution between the Green's function in a semi-infinite medium and $\sigma_{ij}^{(1)}$ on the surface. The corresponding components ($\sigma_{rz}^{(1)}$ and $\sigma_{r\theta}^{(1)}$) can be calculated by convolution between $-p$ and static Green's functions of surface traction for normal traction in a semi-infinite space (Jaeger et al., 2007; Segall, 2010). The Green's functions $g_{xx}^{\sigma z}, g_{xy}^{\sigma z}, g_{yy}^{\sigma z}$ in a Cartesian coordinate system are given by

$$g_{xx}^{\sigma z} = \frac{1}{2\pi}\frac{\mu}{\lambda + \mu}\frac{-x^2 + y^2}{r^4} + \frac{1 + 2\nu}{2}\delta(r), \tag{A.7}$$

$$g_{xy}^{\sigma z} = -\frac{1}{2\pi}\frac{\mu}{\lambda + \mu}\frac{2xy}{r^4}, \tag{A.8}$$

$$g_{yy}^{\sigma z} = \frac{1}{2\pi}\frac{\mu}{\lambda + \mu}\frac{x^2 - y^2}{r^4} + \frac{1 + 2\nu}{2}\delta(r). \tag{A.9}$$

Note that Jaeger et al. (2007) does not include two terms of $\delta(r)$ because they are defined outside the source regions. The two terms can be estimated as the limit of a disk load given by Farrell (1972) as r approaches 0, as shown in the next section. For the convolution between $g_{ij}^{\sigma z}$ and $\sigma_{ij}^{(0)}$, calculation in the wavenumber domain is convenient (Segall,

587   2010). $G_{ij}^{\sigma z}$, which is the Fourier component of $g_{ij}^{\sigma z}$ in the wavenumber domain, is given

588   by

589
$$G_{xx}^{\sigma z} = \frac{1}{2}\frac{\mu}{\lambda+\mu}\frac{-k_x^2+k_y^2}{k_x^2+k_y^2} + \frac{1+2\nu}{2} \tag{A.10}$$

590
$$G_{xy}^{\sigma z} = \frac{1}{2}\frac{\mu}{\lambda+\mu}\frac{-2k_xk_y}{k_x^2+k_y^2} \tag{A.11}$$

591
$$G_{yy}^{\sigma z} = \frac{1}{2}\frac{\mu}{\lambda+\mu}\frac{k_x^2-k_y^2}{k_x^2+k_y^2} + \frac{1+2\nu}{2} \tag{A.12}$$

592

593   Figure A.1 shows a typical example of induced 0th-order stress $\sigma_{zz}^{(0)} - \sigma_{rr}^{(0)}$ and $\sigma_{r\theta}^{(0)}$,

594   which is stress induced by the tsunami wavefield with an azimuthal order of 1 ($\zeta_1^{in} =$

595   1) for Aogashima at 4 mHz. Because $\sigma_{zz}^{(0)} - \sigma_{rr}^{(0)}$ and $\sigma_{r\theta}^{(0)}$ are an order of magnitude smaller

596   than $\sigma_{zz}^{(0)}$ at the surface, we can neglect the first order stress $\sigma_{ij}^{(1)}$. Consequently, the first

597   order displacement $u^{(1)}$ is also negligible. Although the first order correction of normal

598   traction $\sigma_{zz}^{(1)}$ is negligible, those of shear traction, $\sigma_{zx}^{(1)}$ and $\sigma_{zy}^{(1)}$, are significant.
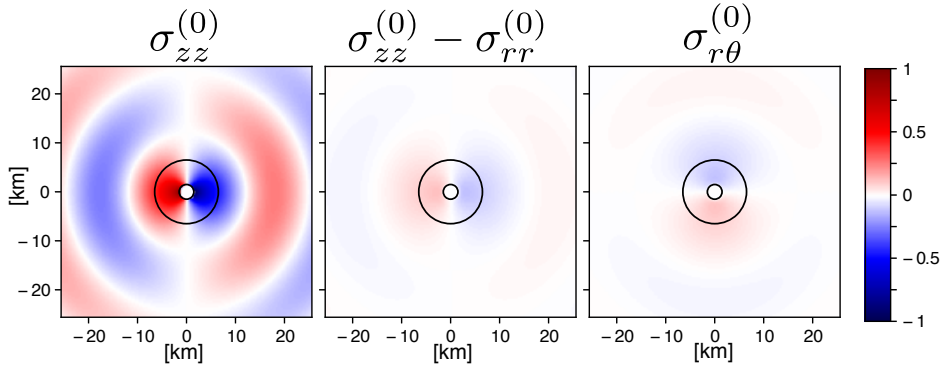

Figure A.1.   Stress σ_{zz} is imposed on the surface. σ_{rr} is the induced principle stress on the surface, which is one order of magnitude smaller than the imposed stress. The inner circle shows the radius of the island at sea level, r_0, and the outer circle shows the radius of the island on the seafloor r_1.

B Stress components by surface loads on a half-space

Stress components by surface loads on a half-space are given Jaeger et al. (2007) as

$$\sigma_{xx} = \frac{1}{2\pi} \left[\frac{3x^2 z}{r^5} + \frac{(1-2\nu)(y^2+z^2)}{r^3(z+r)} - \frac{(1-2\nu)z}{r^3} - \frac{(1-2\nu)x^2}{r^2(z+r)^2} \right] \tag{B.1}$$

$$\sigma_{xy} = \frac{1}{2\pi} \left[\frac{3xyz}{r^5} - \frac{(1-2\nu)xy(z+2r)}{r^3(z+r)^2} \right] \tag{B.2}$$

$$\sigma_{yy} = \frac{1}{2\pi} \left[\frac{3y^2 z}{r^5} + \frac{(1-2\nu)(x^2+z^2)}{r^3(z+r)} - \frac{(1-2\nu)z}{r^3} - \frac{(1-2\nu)y^2}{r^2(z+r)^2} \right]. \tag{B.3}$$

Because the surface values are singular, we derive the simplified form on the surface below.

Let us consider that stress components by a disk load (Love, 1929; Lubarda, 2013) are given by

$$\sigma_{rr} = \frac{p}{2} \begin{cases} 1+2\nu, & r < R \\ -(1-2\nu)\frac{R^2}{r^2}, & r \geq R \end{cases} \tag{B.4}$$

$$\sigma_{\theta\theta}, = \frac{p}{2} \begin{cases} 1+2\nu, & r < R \\ (1-2\nu)\frac{R^2}{r^2}, & r \geq R \end{cases} \tag{B.5}$$

where R is the radius of the disk and p is the pressure applied uniformly over the disk area. The limits of stress as R approaches 0 have the following forms:

$$\sigma_{xx} = \frac{1}{2\pi} \frac{\mu}{\lambda+\mu} \frac{-x^2+y^2}{r^4} + \frac{1+2\nu}{2}\delta(r) \tag{B.6}$$

$$\sigma_{xy} = -\frac{1}{2\pi} \frac{\mu}{\lambda+\mu} \frac{2xy}{r^4} \tag{B.7}$$

$$\sigma_{yy} = \frac{1}{2\pi} \frac{\mu}{\lambda+\mu} \frac{x^2-y^2}{r^4} + \frac{1+2\nu}{2}\delta(r). \tag{B.8}$$

These representations are also given by the limit of equation B.1 as z approaches 0.

References

Aki, K., & Richards, P. G. (1980). *Quantitative Seismology* (Vol. 1). W. H. Freeman, San Francisco.

Amante, C., & Eakins, B. W. (2009). *ETOPO1 Global Relief Model converted to PanMap layer format* [data set]. PANGAEA. doi: 10.1594/PANGAEA.769615

Ardhuin, F., Gualtieri, L., & Stutzmann, E. (2015). How ocean waves rock the Earth: Two mechanisms explain microseisms with periods 3 to 300 s. *Geophys. Res. Lett.*, *42*(3), 765–772. doi: 10.1002/2014GL062782

Ardhuin, F., Rawat, A., & Aucan, J. (2014, may). A numerical model for free infragravity waves: Definition and validation at regional and global scales. *Ocean Model.*, *77*, 20–32. doi: 10.1016/j.ocemod.2014.02.006

Ben-Menahem, A., & Singh, S. J. (2000). *Seismic Waves and Sources* (2nd ed.). Dover Publications, Incorporated.

Bernard, E. N., & Meinig, C. (2011, sep). History and future of deep-ocean tsunami measurements. In *Ocean. mts/ieee kona* (pp. 1–7). IEEE. doi: 10.23919/OCEANS.2011.6106894

Farrell, W. E. (1972). Deformation of the Earth by surface loads. *Rev. Geophys.*, *10*(3), 761. doi: 10.1029/RG010i003p00761

Fujima, K., & Goto, C. (1994). Characteristics of long waves trapped by conical islands, in japanese. *The Japan Society of Civil Engineers*, *1994*(497), 101-110. doi: 10.2208/jscej.1994.497_101

Fukao, Y., Nishida, K., & Kobayashi, N. (2010). Seafloor topography, ocean infragravity waves, and background Love and Rayleigh waves. *J. Geophys. Res. Solid Earth*, *115*(4), 1–10. doi: 10.1029/2009JB006678

Fukao, Y., Sandanbata, O., Sugioka, H., Ito, A., Shiobara, H., Watada, S., & Satake, K. (2018). Mechanism of the 2015 volcanic tsunami earthquake near Torishima, Japan Mechanism of volcanic tsunami earthquake. *Sci. Adv.*.

Gica, E., Spillane, M., Titov, V., Chamberlin, C., & Newman, J. (2008). *Development of the forecast propagation database for NOAA's Short-Term Inundation Forecast for Tsunamis (SIFT)* (Tech. Rep.).

Gill, A. (1982). *Atmosphere-ocean dynamics*. Elsevier Science. Retrieved from https://books.google.co.jp/books?id=8kFPh_SvnAIC

Jaeger, J., Cook, N., & Zimmerman, R. (2007). *Fundamentals of rock mechanics.* Wiley.

Kanamori, H., Ekström, G., Dziewonski, A., Barker, J. S., & Sipkin, S. A. (1993). Seismic radiation by magma injection: An anomalous seismic event near Tori Shima, Japan. *J. Geophys. Res. Solid Earth*, *98*(B4), 6511–6522. doi: 10.1029/92JB02867

Kânoğlu, U., & Synolakis, C. E. (1998). Long wave runup on piecewise linear topographies. *J. Fluid Mech.*, *374*(November 1998), 1–28. doi: 10.1017/S0022112098002468

Kimura, T., Tanaka, S., & Saito, T. (2013). Ground tilt changes in Japan caused by the 2010 Maule, Chile, earthquake tsunami. *Journal of Geophysical Research: Solid Earth*, *118*(1), 406–415. doi: 10.1029/2012JB009657

Krischer, L., Megies, T., Barsch, R., Beyreuther, M., Lecocq, T., Caudron, C., & Wassermann, J. (2015). ObsPy: A bridge for seismology into the scientific Python ecosystem. *Comput. Sci. Discov.*, *8*(1). doi: 10.1088/1749-4699/8/1/014003

Lay, T., Ammon, C. J., Kanamori, H., Yamazaki, Y., Cheung, K. F., & Hutko, A. R. (2011). The 25 October 2010 Mentawai tsunami earthquake (M w 7.8) and the tsunami hazard presented by shallow megathrust ruptures. *Geophys. Res. Lett.*, *38*(6), 2–6. doi: 10.1029/2010GL046552

Liu, P. L.-F., Cho, Y.-S., Briggs, M. J., Lu, U. K., & Synolakis, C. E. (1995). Runup of solitary waves on a circular island. *Journal of Fluid Mechanics*, *302*(10), 259–285. doi: 10.1017/S0022112095004095

Longuet-Higgins, M. S. (1967). On the trapping of wave energy round islands. *J. Fluid Mech.*, *29*(04), 781–821. doi: 10.1017/S0022112067001181

Love, A. E. H. (1929). The Stress Produced in a Semi-Infinite Solid by Pressure on Part of the Boundary. *Philos. Trans. R. Soc. A Math. Phys. Eng. Sci.*, *228*(659-669), 377–420. doi: 10.1098/rsta.1929.0009

Lubarda, V. A. (2013). Circular loads on the surface of a half-space: Displacement and stress discontinuities under the load. *Int. J. Solids Struct.*, *50*(1), 1–14. doi: 10.1016/j.ijsolstr.2012.08.029

Moré, J. J., Sorensen, D. C., Hillstrom, K. E., & Garbow, B. S. (1984). *The MINPACK Project, in Sources and Development of Mathematical Software.* Upper

Saddle River, NJ, USA: Prentice-Hall, Inc.

Nawa, K., Suda, N., Satake, K., Fujii, Y., Sato, T., Doi, K., . . . Shibuya, K.   (2007).
Loading and gravitational effects of the 2004 Indian Ocean tsunami at Syowa
Station, Antarctica.   *Bull. Seismol. Soc. Am.*, *97*(1A), S271–S278.   doi:
10.1785/0120050625

Nishida, K. (2013). Earth's Background Free Oscillations. *Annu. Rev. Earth Planet.*
Sci., *41*(1), 719–740. doi: 10.1146/annurev-earth-050212-124020

Nishida, K.   (2017).   Ambient seismic wave field.   *Proc. Japan Acad. Ser. B*, *93*(7),
423–448. doi: 10.2183/pjab.93.026

Nishida, K., Kawakatsu, H., Fukao, Y., & Obara, K.   (2008, aug).   Background Love
and Rayleigh waves simultaneously generated at the Pacific Ocean floors.   *Geo-*
phys. Res. Lett., *35*(16), L16307. doi: 10.1029/2008GL034753

Okada, Y., Kasahara, K., Hori, S., Obara, K., Sekiguchi, S., Fujiwara, H., & Ya-
mamoto, A.   (2004).   Recent progress of seismic observation networks in Japan
Hi-net, F-net, K-NET and KiK-net.   *Earth, Planets Sp.*, *56*(8), xv–xxviii.   doi:
10.1186/BF03353076

Radhakrishnan, K., & Hindmarsh, A. C.   (1993, dec).   *Description and use of*
LSODE, the Livemore Solver for Ordinary Differential Equations (Tech.
Rep.).   Livermore, CA: Lawrence Livermore National Laboratory (LLNL).
doi: 10.2172/15013302

Rawat, A., Ardhuin, F., Ballu, V., Crawford, W., Corela, C., & Aucan, J.   (2014,
nov).   Infragravity waves across the oceans.   *Geophys. Res. Lett.*, *41*(22),
7957–7963. doi: 10.1002/2014GL061604

Rawlinson, N. (2005). *FMST: Fast Marching Surface Tomography package Research*
(Tech. Rep.). Aust. Natl. Univ.

Rawlinson, N., & Sambridge, M.   (2005).   The fast marching method: An effective
tool for tomographic imaging and tracking multiple phases in complex layered
media. *Explor. Geophys.*, *36*(4), 341–350. doi: 10.1071/EG05341

Rhie, J., & Romanowicz, B.   (2004, sep).   Excitation of Earth's continuous free oscil-
lations by atmosphereoceanseafloor coupling. *Nature*, *431*(7008), 552–556. doi:
10.1038/nature02942

Rodgers, P. W.   (1968).   The response of the horizontal pendulum seismometer to
Rayleigh and Love waves, tilt, and free oscillations of the earth.   *Bull. Seismol.*

Soc. Am., *58*(5), 1385–1406.

Sandanbata, O., Watada, S., Satake, K., Fukao, Y., Sugioka, H., Ito, A., & Shiobara, H. (2017). Ray Tracing for Dispersive Tsunamis and Source Amplitude Estimation Based on Green's Law: Application to the 2015 Volcanic Tsunami Earthquake Near Torishima, South of Japan. *Pure Appl. Geophys.*. doi: 10.1007/s00024-017-1746-0

Satake, K. (2015). Tsunamis. In *Treatise geophys.* (pp. 477–504). Elsevier. doi: 10.1016/B978-0-444-53802-4.00086-5

Satake, K., Fujii, Y., Harada, T., & Namegaya, Y. (2013). Time and space distribution of coseismic slip of the 2011 Tohoku earthquake as inferred from Tsunami waveform data. *Bull. Seismol. Soc. Am.*, *103*(2 B), 1473–1492. doi: 10.1785/0120120122

Satake, K., & Kanamori, H. (1991). Abnormal tsunamis caused by the June 13, 1984, Torishima, Japan, earthquake. *J. Geophys. Res. Solid Earth*, *96*(B12), 19933–19939. doi: 10.1029/91JB01903

Satake, K., Nishimura, Y., Putra, P. S., Gusman, A. R., Sunendar, H., Fujii, Y., . . . Yulianto, E. (2013). Tsunami Source of the 2010 Mentawai, Indonesia Earthquake Inferred from Tsunami Field Survey and Waveform Modeling. *Pure Appl. Geophys.*, *170*(9-10), 1567–1582. doi: 10.1007/s00024-012-0536-y

Segall, P. (2010). *Earthquake and Volcano Deformation.* Princeton University Press.

Smith, R., & Sprinks, T. (1975, nov). Scattering of surface waves by a conical island. *J. Fluid Mech.*, *72*(02), 373. Retrieved from `papers://2ebf624a-5397-4902 -a637-e1c2a5c19c2c/Paper/p1173http://www.journals.cambridge.org/ abstract{\_}S0022112075003424` doi: 10.1017/S0022112075003424

Sorrells, G. G., & Goforth, T. T. (1973). Low-Frequency Earth Motion Generated By Slowly Propagating Partially Organized Pressure Fields. *Bull. Seismol. Soc. Am.*, *63*(5), 1583–1601.

Takagi, R., Nishida, K., Maeda, T., & Obara, K. (2018). Ambient seismic noise wavefield in Japan characterized by polarization analysis of Hi-net records. *Geophys. J. Int.*, *215*(3), 1682–1699. doi: 10.1093/gji/ggy334

Tonegawa, T., Fukao, Y., Shiobara, H., Sugioka, H., Ito, A., & Yamashita, M. (2018). Excitation Location and Seasonal Variation of Transoceanic Infragravity Waves Observed at an Absolute Pressure Gauge Array. *J. Geophys.*

764   *Res. Ocean.*, 40–52. doi: 10.1002/2017JC013488

765 Vogel, R. M., & Shallcross, A. L.   (1996, jun).   The moving blocks bootstrap
766   versus parametric time series models.   *Water Resour. Res.*, *32*(6), 1875–
767   1882.   Retrieved from `http://engineering.tufts.edu/cee/people/vogel/`
768   `documents/moving-blocks.pdfhttp://doi.wiley.com/10.1029/96WR00928`
769   doi: 10.1029/96WR00928

770 Wielandt, E., & Forbriger, T.   (1999).   Near-field seismic displacement and tilt asso-
771   ciated with the explosive activity of Stromboli. *Ann. Geophys.*, *42*(3), 407–416.
772   doi: 10.4401/ag-3723

773 Williams, C. A., & Wadge, G.   (2000).   An accurate and efficient method for includ-
774   ing the effects of topography in three-dimensional elastic models of ground
775   deformation with applications to radar interferometry.   *J. Geophys. Res.*,
776   *105*(B4), 8103–8120. doi: 10.1029/1999JB900307

777 Yuan, X., Kind, R., & Pedersen, H.   (2005).   Seismic monitoring of the Indian Ocean
778   tsunami. *Geophys. Res. Lett.*, *32*(15), L15308. doi: 10.1029/2005GL023464